Journal of Nuclear Materials 389 (2009) 303–310

Contents lists available at ScienceDirect

Journal of Nuclear Materials

journal homepage: www.elsevier.com/locate/jnucmat

Response of strontium titanate to ion and electron irradiation

Y. Zhang [a,*], J. Lian [b], Z. Zhu [a], W.D. Bennett [a], L.V. Saraf [a], J.L. Rausch [a], C.A. Hendricks [a], R.C. Ewing [c], W.J. Weber [a]

[a] Pacific Northwest National Laboratory, P.O. Box 999/MS K8-87, Richland, WA 99352, USA
[b] Department of Mechanical, Aerospace and Nuclear Engineering, Rensselaer Polytechnic Institute, Troy, NY 12180, USA
[c] Department of Geological Sciences, University of Michigan, Ann Arbor, Michigan 48109, USA

A B S T R A C T

The response of strontium titanate ($SrTiO_3$) to ion and electron irradiation is studied at room temperature. For an accurate energy to depth conversion and a better determination of ion-induced disorder profile from Rutherford backscattering spectrometry measurement, a detailed iterative procedure is described and applied to ion channeling spectra to determine the dechanneling yield and the disorder profiles for the Sr and Ti sublattices. The result shows a large underestimation in disorder depth, ~40% at the damage peak, which indicates a large overestimation of the electronic stopping power for 1.0 MeV Au ions in $SrTiO_3$ predicted by the SRIM (Stopping and Range of Ions in Matter) code. Overestimation of heavy ion stopping power may lead to an overestimation of the critical dose for amorphization. The current study also demonstrates possible ionization effects in $SrTiO_3$ under ion and electron irradiation. Pre-amorphized $SrTiO_3$ exhibits strong ionization-induced epitaxial recovery at the amorphous/crystalline interface under electron irradiation.

1. Introduction

Perovskites are the most abundant mineral on earth with a general formula of ABO_3, and strontium titanate ($SrTiO_3$) is a prominent representative of the group. Due to high dielectric constant, good magnetic, ferroelectric and insulating properties, outstanding wear resistance, high resistance against oxidation, and high chemical and thermal stabilities, single crystal $SrTiO_3$ is of technological interest in microelectronics and optoelectronic industries [1–4] and in clean energy research [5–7]. Strontium titanate thin films can be used as insulating layers in dynamic random access memories [2], ferroelectric thin film structures [8,9] and high-T_c superconductor devices [10], potential gate oxide candidates [11], as well as photocatalysts for water splitting [5–7].

Perovskite phases, particularly $SrTiO_3$, have also been proposed as possible ceramic host phases for the immobilization of actinides and some long-lived fission products [12]. The majority of high-level waste (HLW) generated in waste stream from reprocessing of spent nuclear fuel (SNF) is highly radioactive. Immobilization of HLW can be achieved by incorporating it into solid matrices disposed into a deep stabilized geologic repository [13,14]. The potential materials for immobilization of nuclear waste must endure high radiation doses associated with α-decay of the actinides and β-decay of the fission products. Radiation effects in the host phases through atomic displacements and ionization may compromise the physical and chemical durability. Thus, it is important to understand and predict the behavior of these materials in a radiation environment.

In this work, the radiation response of $SrTiO_3$ is studied, as a model system for the perovskite phases. Energetic Au particles are employed to evaluate the damage accumulation through atomic collision. Accuracy of the Stopping and Range of Ions in Matter (SRIM) code is examined. Furthermore, dynamic annealing through ionization under both ion and electron beam (*e*-beam) irradiation is discussed.

2. Experimental procedure

The high-purity single crystal $SrTiO_3$ samples used in this study were obtained from Princeton Scientific Corp. (NJ). The crystals were epi-polished with dimensions of 10 mm × 10 mm × 1 mm and oriented along the [100] axis.

Irradiation of $SrTiO_3$ with 1.0 MeV Au^+ or Au^{2+} ions and subsequent investigation of damage analysis based on ion channeling method were carried out using the 3.0 MV tandem accelerator facilities within the Environmental Molecular Sciences Laboratory (EMSL) at the Pacific Northwest National Laboratory (PNNL) [15]. The crystals were mechanically mounted to a molybdenum plate by molybdenum spring-loaded clips, with a chromel–alumel thermocouple clamped to the sample surface. The crystals were irradiated by 1.0 MeV Au ions at fluences varying from 4×10^{12} cm^{-2} to 5×10^{13} cm^{-2} at room temperature. A large tilt angle of 60° relative to the surface normal was used to produce shallow damage

* Corresponding author.
E-mail address: Yanwen.Zhang@pnl.gov (Y. Zhang).

0022-3115/$ - see front matter © 2009 Elsevier B.V. All rights reserved.
doi:10.1016/j.jnucmat.2009.02.014

that could be readily measured by Rutherford backscattering spectrometry (RBS) in channeling geometry [16] using 2.0 MeV He^+ beam along both the <100>-axial direction and an off-channel (random) direction. A Si detector was located at a scattering angle of 150° relative to the incoming beam.

Electron beam irradiation and *in situ* transmission electron microscopy (TEM) observations were performed using a JEOL 2010F microscope at the University of Michigan operated at 200 kV. Structure and damage recovery were studied by both bright field imaging and selected-area electron diffraction (SAED) patterns. Cross-sectional TEM samples were prepared by the wedge technique using a tripod polisher. Specimens were prepared by pure mechanical polishing, which was followed by ion milling using 4 keV Ar^+ to obtain thin area suitable for TEM observations. Ion milling may induce point defects or create a surface amorphous layer with a thickness of several nm on the thin areas of the TEM samples. However, this surface amorphous layer is much smaller than the typical sample thickness required for high-resolution TEM imaging, and should not have significant effects on the original damage profile induced in $SrTiO_3$ by Au ions.

Time-of-flight secondary ion mass spectrometry (ToF–SIMS) was used to characterize the depth profile of implanted Au ions in the $SrTiO_3$ samples. An IONTOF V spectrometer (IONTOF GmbH, Münster, Germany) was used in the ToF-SIMS measurement. A dual-beam depth profile strategy was employed. The sputtering beam was 2 keV Cs^+ with a scan area of 300 μm × 300 μm. The analysis beam was 25 keV Bi^+ ions, which were focused into ~2 μm diameter and rastered at the center of the sputtering crater with a scan area of 100 μm × 100 μm during data acquisition. The base pressure of the analysis chamber was 2×10^{-10} mbar. The implanted Au profiles were measured by SIMS assuming a constant sputtering rate that was determined by profilometry measurements. The depth of each square crater resulting from the SIMS measurements was determined by both ZYGO NewView 200 and Dektak 6 M profilometers. The ZYGO microscope is a general purpose optical profilometer with 3D imaging features. This non-destructive and non-contact technique determines depth from the difference between two focal planes by precise z-movement of the lens. Since the $SrTiO_3$ substrate is partially transparent, the reflected light from other planes may make it difficult for the instrument to detect the correct focal plane. Thus, depths of all craters were also confirmed by the Dektak profilometer utilizing a 12.5 μm diamond-tipped stylus that is in physical contact with the sample surface. Good agreement was found between the two profilometer depth measurements.

3. Results and discussion

3.1. Damage evolution and amorphization by atomic collision

Due to high radiotoxicity and long life, actinide disposal is certainly the most challenging task. Alpha decay of actinide elements produces high-energy alpha particles and low-energy heavy recoil nuclei (alpha recoils) [12]. The alpha particles, due to smaller mass, have relatively less radiation impact. The heavy alpha recoils account for most of the crystal damage produced through elastic scattering collisions. Accumulation of alpha decay damage may lead to serious disorder or even a crystalline to amorphous transition. Such phase transformation may enhance the ceramic aqueous dissolution and produce a large swelling leading to cracks or even fragmentation of the waste form. Since both effects may increase the actinide release, it is important to understand and predict the behavior of the materials in a radiation environment.

As possible ceramic host phases for the immobilization, disorder induced by recoil nuclei in $SrTiO_3$ has been studied by heavy ion irradiation [14–24]. Since nuclear stopping at the damage peak resulting from heavy ion irradiation, such as Au and Pb, is similar to the nuclear stopping of alpha recoils (~ 5 keV/nm), the damage evolution at the damage peak under heavy ion irradiation provides a reasonable simulation of the damage evolution behavior due to alpha recoil collision cascades. To characterize and evaluate the material response under different irradiation conditions, dose in displacements per atom (dpa) is commonly used [12–17,19–22], and defect production and damage evolution are studied and analyzed as a function of dpa. The SRIM code, as one of the most accepted simulation programs, is widely used for calculating stopping power and ion range in matter [25,26]. Since the stopping prediction from SRIM is based on fits to experimental data, it usually provides reasonable predictions. In the newly released version SRIM 2008 [26], the average accuracy of the stopping powers is stated to be 4.8% overall. It further points out that the experimental stopping powers for heavy ions contain far more uncertainties than that for light ions. For light ions of H and He, more than 74% of data points are within 5% of the SRIM predictions and 87% within 10%. For heavy ions, more than 58% within 5% and 82% within 10%. The larger error for heavy ions is partly due to limited experimental data as well as the increased scatter of the data points.

In this section, damage evolution and amorphization of $SrTiO_3$ by atomic displacement are investigated under 1 MeV Au ion irradiation. The ion-induced damage profile is determined using an iterative procedure. The accuracy of the SRIM predictions is examined by comparing the predicted damage profile and Au distribution to the experimental results.

3.1.1. RBS spectra and damage profiles

Channeling RBS spectra along the <100> direction in $SrTiO_3$ are shown in Fig. 1 for the samples irradiated at different Au ion fluences. The random and channeling spectra from a virgin area are also included, which indicate the fully amorphous and essentially defect-free states, respectively. The ratio of the backscattering yield in the virgin spectrum to the yield in the random spectrum just below the surface peak is 1.9%, which indicates the high quality of the crystal. As shown in Fig. 1, the increase in disorder on the Sr and Ti sublattices with increasing ion fluences is evident. At high fluences, the peak height reaches the random level, indicating that a fully amorphous state is reached based on ion-channeling criteria.

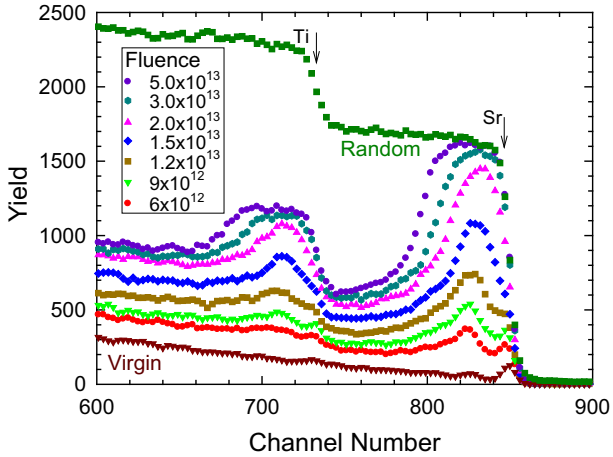

Fig. 1. A series of <100>- aligned RBS spectra for $SrTiO_3$ irradiated under 1.0 MeV Au irradiation at room temperature to different ion fluences from 6×10^{12} cm^{-2} (bottom) to 5×10^{13} cm^{-2} (top). Random and channeling spectra from a virgin area are also included. Backscattered He ions from the sample surface are marked for the Sr and Ti sublattices, respectively. For visual clarity, every three data points are shown.

Depth profiles of the relative disorder on the Sr and Ti sublattices can be obtained from the RBS spectrum in Fig. 1 by applying an iterative procedure [21,27–29]. Analysis examples are shown in Figs. 2–4 for the specimens implanted to 5.0×10^{13} cm^{-2} and 1.5×10^{13} cm^{-2}, which illustrates the general analysis procedures for all the spectra. For each ion fluence, a set of three spectra is needed to determine the corresponding disorder profile, as shown in Fig. 2 for the 5.0×10^{13} cm^{-2} implanted sample that contains (1) the measured channeling spectrum from the irradiated sample, (2) the virgin spectrum and (3) the random spectrum. To reduce the uncertainty, a curve fit is used to fit the random spectra, as shown by the solid line in Fig. 2. The dashed line is the extrapolation of the random yield from the Sr sublattice to lower channels. The height difference between the solid line and the dashed line is the random yield from the Ti sublattice. Normalized to the fitted random spectrum in Figs. 2, Figs. 3(a) and 4(a) show the normalized virgin spectrum, $V(x)$, and the normalized channeling spectrum, $\eta(x)$, for the 5.0×10^{13} cm^{-2} and the 1.5×10^{13} cm^{-2} implanted samples, respectively. The dechanneling component, $R(x)$, starts from a point on the virgin spectrum near the beginning of the damaged region and may stop at a point beyond the damage region. In the cases shown in Figs. 3(a) and 4(a), $R(x)$ starts just after the surface peak at channel 842, and stops at channel 600, fully covers the region of interests. The iterative procedure can be followed as:

$$R(842) = V(842) + [1 - V(842)] \times \left(1 - \exp\left[-\sigma_D \times \left(\frac{\eta(843) - R(843)}{1 - R(843)}\right)\right]\right).$$

Where the dechanneling component $R(843)$ is assumed to be zero. At the next channel (841), the dechanneling function, $R(841)$ can be determined as

$$R(841) = V(841) + [1 - V(841)] \times \left(1 - \exp\left\{-\sigma_D \times \left[\left(\frac{\eta(843) - R(843)}{1 - R(843)}\right) + \left(\frac{\eta(842) - R(842)}{1 - R(842)}\right)\right]\right\}\right).$$

The iterative procedure successively moves in depth to the next channel to determine the dechanneling function, $R(x)$, which enables the separation of the direct backscattering contribution from the displaced atoms at that depth

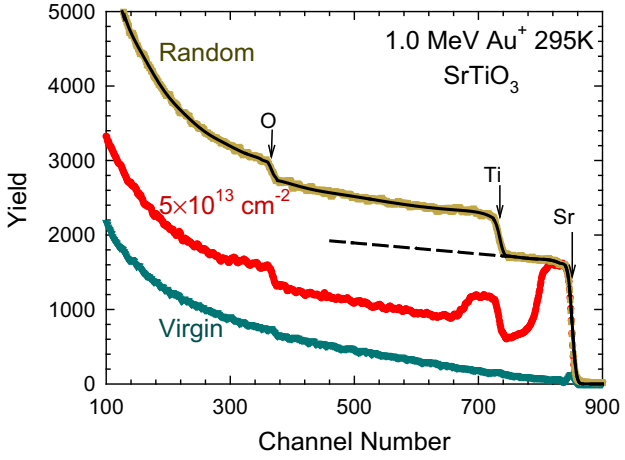

Fig. 2. RBS spectra along <1 0 0> direction in $SrTiO_3$ for the virgin sample and the sample irradiated by 1.0 MeV Au ions to 5×10^{13} cm^{-2}, together with the random spectrum. A curve fit of the random spectrum is shown by the solid line. The dashed line is the extrapolation of the random yield from the Sr sublattice to lower channels.

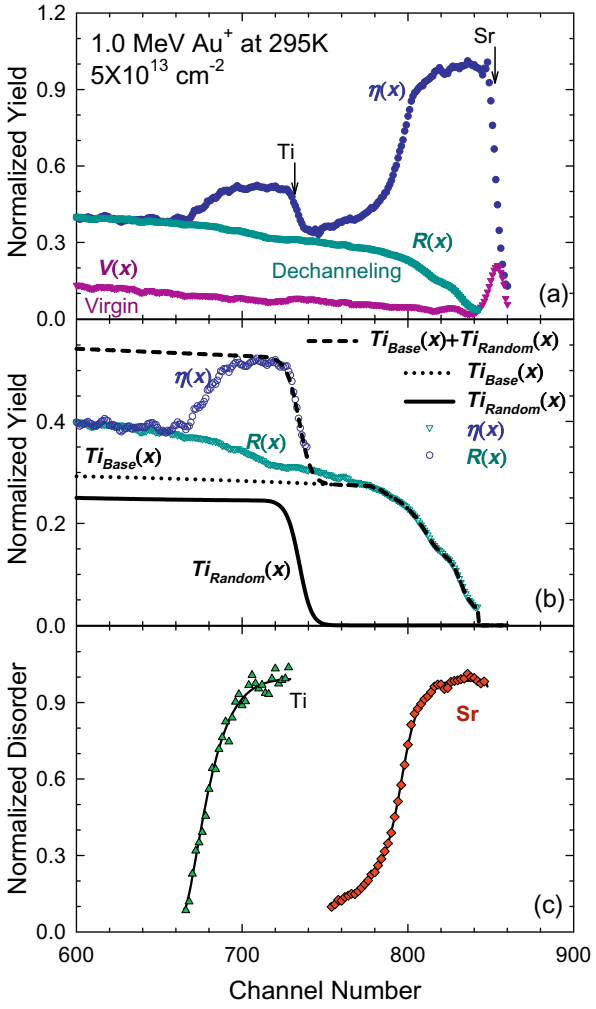

Fig. 3. Analysis of Au-induced damage on both the Sr and Ti sublattices for the 5×10^{13} cm^{-2} irradiated sample. (a) The normalized channeling spectra, $\eta(x)$, and the virgin spectrum, $V(x)$. The dechanneling function, $R(x)$, is determined from the iterative procedure. Backscattered He ions from the sample surface are marked for the Sr and Ti sublattices, respectively. (b) The normalized channeling spectrum, $\eta(x)$; and the dechanneling spectrum, $R(x)$; the dechanneling yield from the Sr sublattice, $Ti_{Base}(x)$ (dotted line); the random spectrum of the Ti sublattice $Ti_{Random}(x)$ (solid line) superimposed on top of the dechanneling yield from the Sr sublattice, $Ti_{Base}(x) + Ti_{Random}(x)$ (dashed line). (c) The relative disorder for both the Sr and Ti sublattices determined using the iterative procedure.

$$R(x) = V(x) + [1 - V(x)] \times \left(1 - \exp\left[-\sigma_D \times \sum_{x+1}^{843}\left[\left(\frac{\eta(x+1) - R(x+1)}{1 - R(x+1)}\right)\right]\right]\right).$$

The parameter, σ_D, is the only adjustable parameter that is related to dechanneling cross section for the disorder along the axial channel direction. Although the dechanneling mechanisms are not thoroughly understood, the value of σ_D can be determined when the dechanneling component $R(x)$ overlaps with the normalized channeling spectrum $\eta(x)$ after the damage peak, as shown in Figs. 3(a) and 4(a) at channel from 600 to 660. After separation of the dechanneling component from the direct backscattering contribution, $\eta(x) - R(x)$, the profile of the relative Sr disorder is then derived by $[\eta(x) - R(x)]/[1 - R(x)]$. The determination of the disorder level on the Ti sublattice is more challenging due to the overlap with the backscattering yield from the Sr sublattice. The general procedure is demonstrated in Figs. 3(b) and 4(b). The solid line is the random yield from the Ti sublattice, $Ti_{Random}(x)$, which is

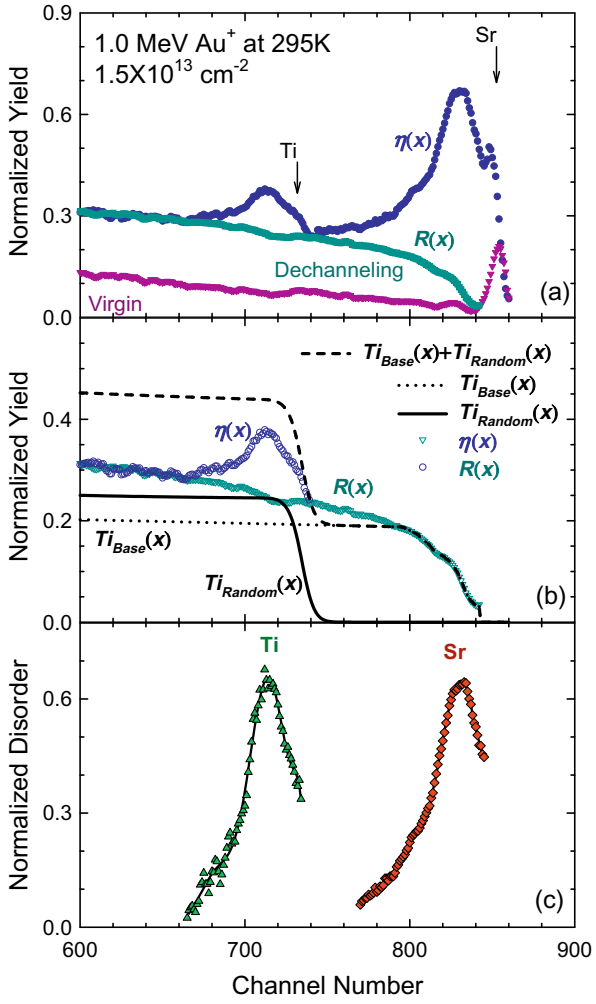

Fig. 4. Analysis of Au-induced damage on both the Sr and Ti sublattices for the 1.5×10^{13} cm^{-2} irradiated sample. (a) The normalized channeling spectra, $\eta(x)$, and the virgin spectrum, $V(x)$. The dechanneling function, $R(x)$, is determined from the iterative procedure. Backscattered He ions from the sample surface are marked for the Sr and Ti sublattices, respectively. (b) The normalized channeling spectrum, $\eta(x)$; and the dechanneling spectrum, $R(x)$; the dechanneling yield from the Sr sublattice, $Ti_{Base}(x)$ (dotted line); the random spectrum of the Ti sublattice $Ti_{Random}(x)$ (solid line) superimposed on top of the dechanneling yield from the Sr sublattice, $Ti_{Base}(x) + Ti_{Random}(x)$ (dashed line). (c) The relative disorder for both the Sr and Ti sublattices determined using the iterative procedure.

determined by the difference between the solid and dashed lines from the random spectrum as indicated in Fig. 2. The base line spectrum for the Ti sublattice, $Ti_{Base}(x)$, is attributed to the dechanneling contribution resulting from the Sr disorders, as shown by the dotted lines in Figs. 3(b) and 4(b) for the 5.0×10^{13} cm^{-2} and the 1.5×10^{13} cm^{-2} implanted samples, respectively. The relative Ti disorder is then derived by $[\eta(x) - R(x)]/[Ti_{Random}(x) + Ti_{Base}(x) - R(x)]$, where the sum of $Ti_{Random}(x)$ and $Ti_{Base}(x)$ is shown as the dashed line in Figs. 3(b) and 4(b). The corresponding disorder profiles on both the Sr and Ti sublattices are shown in Figs. 3(c) and 4(c) for the 5.0×10^{13} cm^{-2} and the 1.5×10^{13} cm^{-2} implanted samples, respectively. Since the dechanneling component overlaps with the normalized channeling spectrum after the damage peak where $\eta(x) - R(x) = 0$, the displacement density fall to zero as shown in Figs. 3(c) and 4(c).

It should point out that the backscattering yield from the disorder of the Ti sublattice is superimposed on that from the disorder of the Sr sublattice, as shown in Fig. 1, which may lead to increased uncertainty for determining the Ti disorder profiles. Due to limited separation of the damage peak from the Sr and Ti sublattices in RBS, determination of $Ti_{Base}(x)$ may also lead to a relatively larger uncertainty. Accurate determination of $Ti_{Base}(x)$ is expected when the damage peak is narrow and there is a clear separation between the damage peaks from different sublattices. In this work, the disorder profiles of the Sr sublattice are more reliable, as compared to the disorder profiles of the Ti sublattice. The iterative procedure demonstrated in Figs. 2–4 is, however, valid for analyzing RBS spectra of compound targets. It provides a more reliable determination of the dechanneling profiles, as compared with a linear subtraction, and therefore a more reliable determination of the disorder profiles [21].

The disorder profiles on the Sr and Ti sublattices under different irradiation fluences are determined using the iterative procedure, and the results are summarized in Fig. 5. The depth scale in nm is determined by the energy difference at each channel and the He ion stopping in $SrTiO_3$ from the SRIM 2008 simulations [25,26] under the assumptions of a sample density of 5.118 g cm^{-3} (8.4×10^{22} at cm^{-3}). As ion fluence increases, the disorder increases over the whole irradiation depth on both sublattices, eventually achieving an amorphous state. Further irradiation results in a buried amorphous layer that expands toward the surface and deeper into the bulk. Within the experimental uncertainties, the results in Fig. 5 show similar disorder profiles on the Sr and Ti sublattices at each ion fluence. While the damage level clearly increases with irradiation fluence, the peak position moves progressively to the surface, as shown by the dashed lines in Fig. 5, which indicates that, for the medium and highly damaged samples, irradiation-induced surface sputtering, composition change or density change may not be negligible.

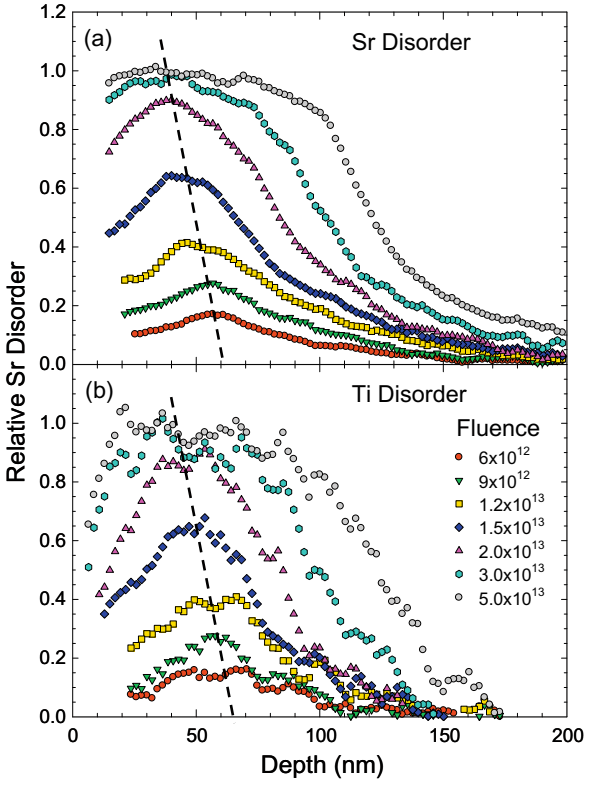

Fig. 5. Disorder profiles on (a) Sr and (b) Ti sublattices after irradiation to different ion fluences from 6×10^{12} cm^{-2} to 5×10^{13}. The profiles are obtained from the spectra shown in 1 by applying the iterative procedure described in Figs. 2–4. The damage peak moves progressively to the surface, as marked by the dashed lines.

3.1.2. Large deviation between SRIM predicted profiles and the experimental results

Damage profile in dpa and Au distribution are determined by the SRIM 2008.01 full-cascade simulations [26] under the assumptions of a sample density of 5.118 g cm^{-3} and threshold displacement energies of 45, 70, and 80 eV for O [30,31], Ti [32] and Sr [32], respectively. The SRIM predicted damage profile is determined from the sum of the predicted vacancy concentration of Sr, Ti and O and the replacement collisions, as shown in Fig. 6(a) from 5×10^{12} cm^{-2} irradiation.

The depth in nm can be calculated from the energy differences (in keV) between the initial energy of the ions scattered from sample surface and the energy of the ions scattered at a certain depth that strike the detector. As indicated at the SRIM webpage [26], more accurate stopping prediction is normally the case for light ions, while heavy ion stopping may contain larger error. Since the SRIM predicted electronic stopping power for He in $SrTiO_3$ is used to convert energy differences, accurate electronic stopping power values are essential to the reliable determination of both damage profile and Au distribution from the RBS measurements. Good He stopping predictions from the SRIM code have been validated experimentally in Si [33], Au [34], SiC [35,36] and a few oxides [37–39], which provide some confidence of using the SRIM predicted He stopping in $SrTiO_3$.

The comparisons of the SRIM predictions and the experimental results of the damage profiles and the Au ion distribution are shown in Fig. 6. To avoid possible impact from ion beam modification, the damage profiles of three low-fluence irradiated samples are used for comparisons in Fig. 6(a). As the irradiation fluence increases from 4×10^{12} to 9×10^{12} cm^{-2}, the overall disorder increases. The corresponding damage peak occurs at ~53 nm for the lowest fluence sample, and at ~ 56 nm for the 6×10^{12} cm^{-2} and 9×10^{12} cm^{-2} samples, as marked on the plot. The relatively lower stopping power of channeled He ions for the 4×10^{12} cm^{-2} irradiated sample may be the primary cause for this small shift. Reduction of stopping power along channeling direction has been reported for light ions in Si [40] and SiC [41,42]. As damage level increases with the ion fluence, the stopping power along channeling directions gets close to the random stopping power. Considering the reduction of the stopping power along the channeling direction, the actual damage profile may be slightly deeper than what is shown in Fig. 6(a). The SRIM predicted damage peak in a random material occurs at 39 nm, much shallower than the experimental results with difference close to 40%. Another clear disagreement in Fig. 6(b) is the Au profile predicted by the SRIM calculation and measured by SIMS. The Au profile measured by SIMS is peaked around 86.5 nm with a full width at half maximum (FWHM) of 102 nm, where the SRIM predicts the peak at 71.5 nm with a FWHM of 77 nm. Comparing the measured values with the SRIM prediction, the measured Au peak is 21% deeper than the depth that is predicted by SRIM. The deviations shown by the damage profiles and the Au ion distribution are attributed to the overestimation of the electronic stopping of the SRIM prediction.

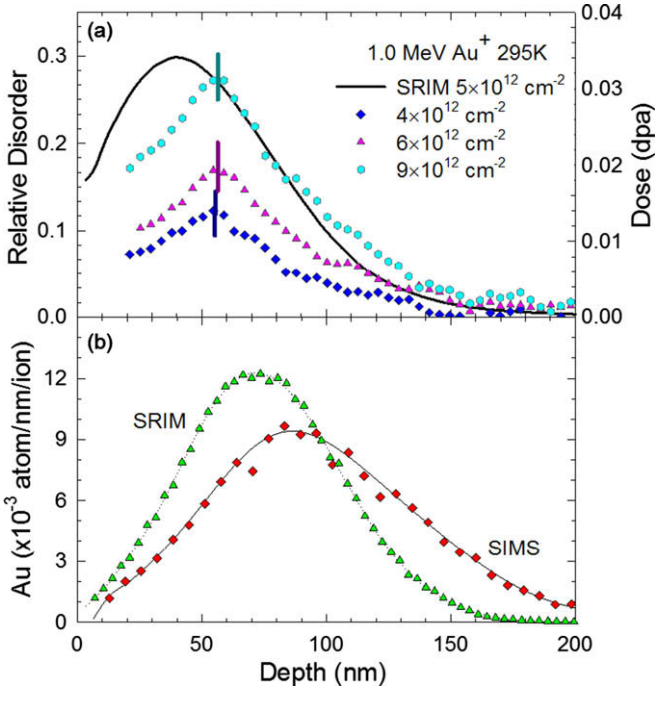

Fig. 6. Comparison of the SRIM predictions to the experimental results. (a): the damage profile in dpa (right *y*-axis) predicted by the SRIM simulation at ion fluence of 5×10^{12} cm^{-2} is shown as the solid line. The damage profiles (left *y*-axis) of the samples irradiated to ion fluences of 4×10^{12}, 6×10^{12} and 9×10^{12} cm^{-2} measured by ion channeling are shown as the data points, where the peak positions are marked by the short lines. Small shift of the peak position to a deeper depth is observed with increasing ion fluences. (b) The Au distribution in the unit of atom per nm per ion predicted by SRIM (triangles) and measured by SIMS (diamonds). The lines are curve fit to guide the eye.

3.2. Heavy ion stopping

Despite intense research in penetration of charged particles in solids over almost a century, electronic stopping power is not adequately described, particularly in the case of heavy ions in compound targets. Limited experimental data have shown large discrepancies [43,44]. Only a few ion-target combinations have been studied in sufficient detail to allow interpolation and extrapolation on purely experimental grounds. Available theories [43–48]) predict stopping powers that are in varying levels of agreement with limited experimental data. As pointed out at the international symposium in 2006 on *Ion Beam Science: Solved and Unsolved Problems* [49], current theories for swift heavy ion stopping (>Bohr velocity, v_0) are still under development, and theories for low-velocity stopping ($<v_0$) in insulators are essentially nonexisting. The passage of a heavy ion through a solid material represents a strong intrusion that cannot generally be described adequately as a weak perturbation of the medium, as is commonly assumed in the quantification of electron and proton penetration. Moreover, heavy ions are composite particles carrying electrons except at high velocity, and their interaction with bound and free electrons in the stopping medium is a problem of considerable complexity involving a number of processes that are absent or less significant in the case of light projectiles.

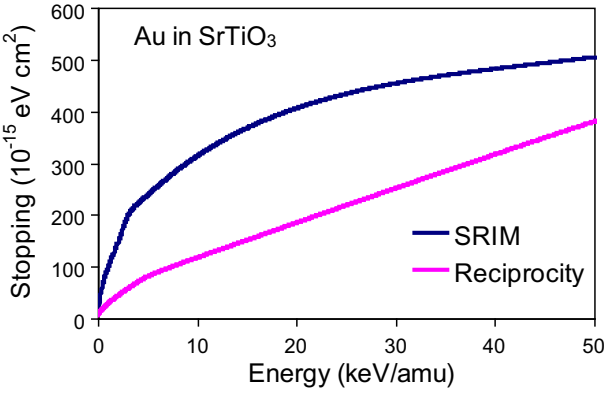

Fig. 7. Comparison of electronic stopping power predicted by the SRIM code and the reciprocity principle. The large deviation is evident.

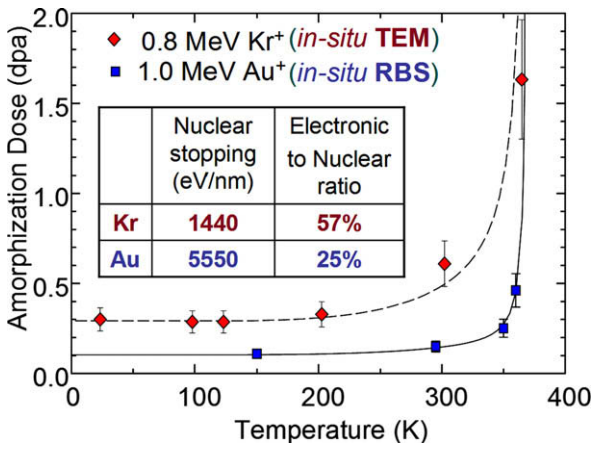

Fig. 8. Temperature dependence of the critical dose for amorphization under Kr [52] and Au irradiation that are observed by TEM and RBS, respectively. The nuclear stopping and the ratio of electronic stopping to nuclear stopping at relevant energies (800 keV for Kr ions and 400 keV for Au ions) at which the critical dose for amorphization is determined are summarized in the table as inset.

Although it is not possible to provide reliable stopping predictions for Au in $SrTiO_3$ from this work, a recent study [50] has suggested that, as the first estimation, the stopping cross section may be determined from the inverted ion-target system by applying the concept of reciprocity. The principle of reciprocity is based on the invariance of the inelastic excitation in ion-atom collisions against interchange of projectile and target of low-velocity ions in matter, such as in the case of 1.0 MeV Au ions in $SrTiO_3$ in the current study. The electronic stopping cross sections in the unit of 10^{-15} eV cm^2 for Sr, Ti and O in Au are calculated from the SRIM 2008 code, the total electronic stopping cross section for Au in $SrTiO_3$ can then be determined by applying the Bragg's rule. The electronic stopping powers predicted by the SRIM code and by the reciprocity approach are shown in Fig. 7. Below 5 MeV (~25 keV/amu), the SRIM predicted values are about twice much as the value based on the reciprocity approach. As particle energy increases, the deviation between the two predictions decreases. However, the SRIM predicted stopping is still ~1/3 higher than the value predicted by the reciprocity approach at 10 MeV (~50 keV/amu). While the applicability of the reciprocity approach needs to be validated [50], the large overestimation of the SRIM predicted electronic stopping powers should not be neglected. Overestimation of heavy ion stopping power may lead to overestimated critical dose for amorphization, or underestimated the projectile range. Due to the importance of $SrTiO_3$ material, attention should be taken into account when studying or predicting ion radiation effects for device and nuclear applications.

3.3. Ionization effects in $SrTiO_3$ under ion and electron irradiation

The critical dose for amorphization is the dose when a continuous amorphous layer starts to develop. From the RBS channeling criteria, the critical dose for amorphization is defined when the channeling spectrum just overlaps with the random spectrum, as shown in Fig. 1, or when the relative disorder reaches 1.0, as shown in Fig. 5 for the 3.0×10^{13} cm^{-2} irradiated sample. A number of studies have been carried out to characterize the critical dose for amorphization using Au [20], Pb [18], Xe [51] and Kr ions [52]. The critical dose for amorphization was previously determined under Au and Kr ion irradiation at difference temperatures, and a

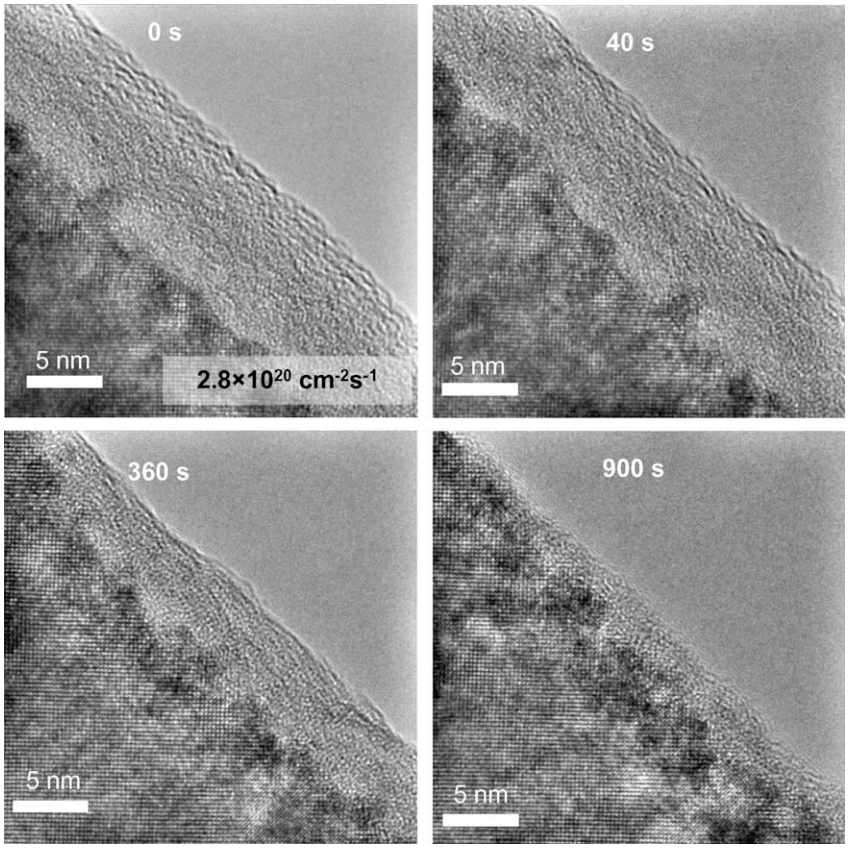

Fig. 9. High resolution TEM images showing the a/c interface motion under *e*-beam exposure with flux of 2.8×10^{20} cm^{-2} s^{-1}. The thickness of the pre-amorphized layer reduces from ~8.6 nm to ~1.5 nm after 900 s electron beam irradiation.

comparison is shown in Fig. 8. A much higher amorphization dose is determined by TEM observation under the Kr ion irradiation [52], as compared to the RBS results under Au ion irradiation [20]. As demonstrated in Sections 3.1 and 3.2, there is an overestimation of the electronic stopping power for Au ions in $SrTiO_3$, which leads to an overestimation of the critical dose for amorphization, and therefore there exists an even larger deviation in Fig. 8. This difference was previously attributed to a few possible contributions, including difference in definition of the dose for amorphization by RBS and TEM techniques, the uncertainties in ion fluence measurements, and the effects of ion mass [20]. For the TEM observation, typical thickness of a TEM specimen is a few tens nm to – a hundred nm. Kr ions interact with the target atoms at the energy close to its original energy of 800 keV, where nuclear stopping is less dominant, and the ratio of electronic stopping to nuclear stopping is high. For the Au ion irradiation, the amorphization is determined by RBS at the damage peak region with ion energy slowing down to ~400 keV, where the nuclear stopping power is dominant and the ratio of electronic stopping to nuclear stopping is low. Since ion-solid interaction leads to significant production of electron-hole pairs through electronic energy deposition in the vicinity of the defects, local electronic excitations and relaxations of the electron-hole pairs can have a major effect on the kinetics of atomic processes in many materials [53]. The nuclear stopping and the ratio of electronic to nuclear stopping at relevant energy at which the critical dose for amorphization is determined are summarized in Fig. 8. Comparing the values in the inset, the Au irradiation has close to four times higher nuclear energy deposition density than the Kr irradiation; however, the ratio of the electronic to nuclear stopping is more than two times lower (twice less the electron-hole pairs). The large deviation in Fig. 8 may indicate a notable ionization effect under ion irradiation.

Another possible contribution to the deviation shown in Fig. 8 may result from the instantaneous *e*-beam-enhanced annealing and/or recrystallization under the TEM observation. The *e*-beam-enhanced ionization effects were investigated using a pre-amorphized $SrTiO_3$ surface layer under electron flux of 2.8×10^{20} and $7.8 \times 10^{20}\ cm^{-2}\ s^{-1}$, both are commonly used electron flux for TEM observations. As shown in Figs. 9 and 10, under exposure to 200 keV electron beam within the TEM, the amorphous layer thickness decreases as the amorphous/crystalline (a/c) interface moves

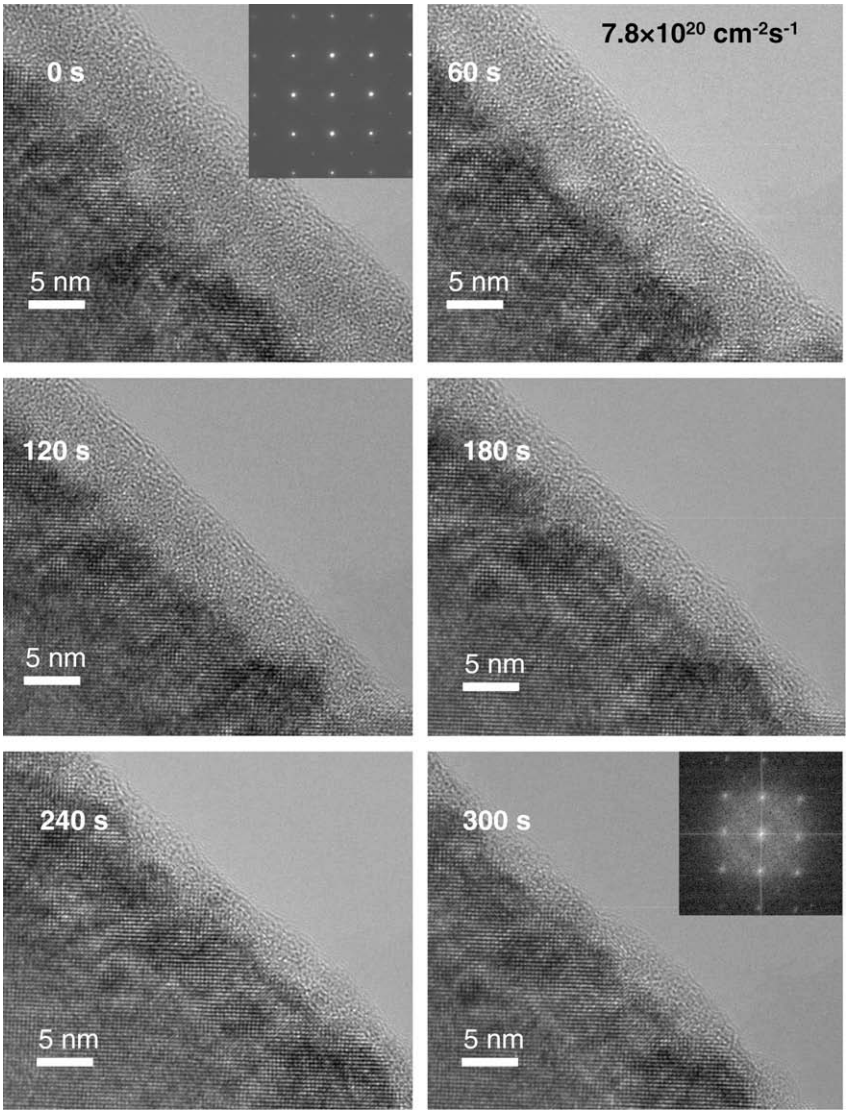

Fig. 10. High resolution TEM images showing the a/c interface motion under *e*-beam exposure with flux of $7.8 \times 10^{20}\ cm^{-2}\ s^{-1}$. The thickness of the pre-amorphized layer reduces from ~6.9 to ~1.7 nm after 300 s electron beam irradiation. Also included are the insets of SAED patterns taken from the virgin region (top) and recrystallized region (bottom).

toward the surface with prolonged exposure time. The SAED patterns in Fig. 10 have also confirmed the epitaxial recrystallization under e-beam irradiation. Furthermore, fast recrystallization can be achieved under more intense electron irradiation as indicated by much short exposure time in Fig. 10. One may notice that the starting thickness of the amorphous layer in Fig. 9 is ~8.6 nm, which is thicker than the layer of ~6.9 nm observed in Fig. 10 at 0 s. This was due to fast annealing under the *e*-beam when the HRTEM image was taken under 7.8×10^{20} cm^{-2} s^{-1} electron beam exposure.

It is noticeable that the *e*-beam flux during the TEM observation is on the order of 10^{20} cm^{-2} s^{-1}, eight order magnitudes higher than the ion flux during the ion irradiation. It is worth to pointing out that electrons deposit ionizing energy more uniformly over the irradiated area that contains pre-existing ion damages; ions, however, deposit electronic energy in the vicinity of the ion track with diameter of a few nm during the dynamic atomic displacement processes. Although it is difficult to quantify the impact of the ionization-induced dynamic recovery due to inelastic scattering processes, significant annealing/recrystallization under the *e*-beam irradiation can not be neglected under TEM observation.

4. Conclusions

Response of $SrTiO_3$ to ion and electron irradiation is studied. The damage profiles produced by 1.0 MeV Au ions are investigated by RBS channeling technique. Quantitative analysis of disorder profiles from the RBS channeling measurement is described. An iterative procedure is applied to separate the backscattered dechanneled particle from the particles that are backscattered from the displaced atoms. The resulting disorder profiles from the RBS measurements are deeper than the SRIM predicted profiles. Large overestimation of the stopping power by the SRIM predictions is also shown from the Au distribution. Ionization effects on determination of critical dose for amorphization are clearly observed, where electronic energy deposition from either ion irradiation or electron irradiation plays important roles during dynamic or post-defect annealing. The possible impacts due to stopping error and ionization effects need to be taking into account when studying damage accumulation as a function of dpa, or comparing radiation behavior, such as mass effects and critical dose for amorphization resulting from different irradiation.

Acknowledgements

This work was supported by the Division of Materials Science and Engineering, Office of Basic Energy Sciences, US Department of Energy. Experiments were performed at EMSL, a national scientific user facility sponsored by the Department of Energy's Office of Biological and Environmental Research and located at Pacific Northwest National Laboratory. Pacific Northwest National Laboratory is operated by Battelle for the US Department of Energy under Contract No. DE-AC05-76RL01830. J. Lian and R.C. Ewing acknowledge support from the Office of Basic Energy Sciences, US Department of Energy under Grant DE-FG02-97ER45656.

References

[1] N. Erdman, K.R. Poeppelmeler, M. Asta, O. Warschkow, D.E. Ellis, L.D. Marks, Nature 419 (2002) 55.
[2] G.D. Wilk, R.M. Wallace, J.M. Anthony, J. Appl. Phys. 89 (2001) 5243.
[3] K. Oyoshi, S. Hishita, H. Haneda, J. Appl. Phys. 87 (2000) 3450.
[4] M. Kiyotoshi, E. Kazuhiro, Appl. Phys. Lett. 67 (1995) 2468.
[5] F.T. Wagner, G.A. Somorjai, Nature 285 (1980) 559.
[6] H. Mizoguchi, K. Ueda, M. Orita, S.C. Moon, K. Kajihara, M. Hirano, H. Hosono, Mater. Res. Bull. 37 (2002) 2401.
[7] Akihiko Kudo, Int. J. Hydrogen Energ. 31 (2006) 197.
[8] M. Takesada, M. Itoh, T. Yagi, Phys. Rev. Lett. 96 (2006) 227602.
[9] S.L. Swartz, IEEE Trans. Insul. 25 (1990) 935.
[10] C. Aruta, Phys. Status Solidi A 183 (2001) 353.
[11] A. Kosola, M. Putkonen, L.-S. Johansson, L. Niinistö, Appl. Surf. Sci. 211 (2003) 102.
[12] W.J. Weber, R.C. Ewing, C.R.A. Catlow, T. Diaz de la Rubia, L.W. Hobbs, C. Kinoshita, Hj. Matzke, A.T. Motta, M.A. Nastasi, E.H.K. Salje, E.R. Vance, S.J. Zinkle, J. Mater. Res. 13 (1998) 1434.
[13] R.C. Ewing, W.J. Weber, J. Lian, J. Appl. Phys. 95 (2004) 5949.
[14] C. Sabathier, J. Chaumont, S. Rouzière, A. Traverse, Nucl. Instrum. and Meth. B 234 (2005) 509.
[15] S. Thevuthasan, C.H.F. Peden, M.H. Engelhard, D.R. Baer, G.S. Herman, W. Jiang, Y. Liang, W.J. Weber, Nucl. Instrum. and Meth. Phys. Res. A 420 (1999) 81.
[16] W. Chu, J.W. Mayer, M. Nicolet, Backscattering Spectrometry, Academic Press, New York, 1978.
[17] S. Soulet, J. Chaumont, C. Sabathier, J.-C. Krupa, J. Mater. Res. 17 (2002) 9–13.
[18] C. Sabathier, J. Chaumont, J.C. Krupa, Nucl. Instrum. and Meth. B 226 (2004) 556.
[19] C. Sabathier, J. Chaumont, J.-C. Krupa, Nucl. Instrum. and Meth. B 196 (2002) 308.
[20] Y. Zhang, J. Lian, C.M. Wang, W. Jiang, R.C. Ewing, W.J. Weber, Phys. Rev. B 72 (2005) 094112.
[21] Y. Zhang, W.J. Weber, V. Shutthanandan, S. Thevuthasan, Nucl. Instrum. and Meth. B 251 (2006) 127.
[22] Y. Zhang, C.M. Wang, M.H. Engelhard, W.J. Weber, J. Appl. Phys. 100 (2006) 113533.
[23] R.B. Greegor, F.W. Lytle, G.W. Arnold, R.C. Ewing, J. Non-Cryst. Solids 122 (1990) 121.
[24] T. Monteiro, M.J. Soares, C. Boemare, E. Alves, J.G. Correia, Radiat. Eff. Def. Solids 157 (2002) 1071.
[25] J.F. Ziegler, J.P. Biersack, M.D. Ziegler, The Stopping and Range of Ions in Solids, SRIM Co., 2008 (as well as the original book by J.F. Ziegler, J.P. Biersack, U. Littmark, Pergamon, New York, 1985).
[26] J.F. Ziegler, SRIM-2008, v. 2008.40. <http://www.srim.org>.
[27] M.L. Swanson, in: J.R. Tesmer, M. Nastasi (Eds.), Handbook of Modern Ion Beam Materials Analysis, Materials Research Society, Pittsburgh, PA, 1995, p. 263.
[28] J.S. Williams, R.G. Elliman, in: J.R. Bird, J.S. Williams (Eds.), Ion Beams for Materials Analysis, Academic Press, Australia, 1989, p. 286.
[29] L.C. Feldman, J.W. Mayer, S.T. Picraux, Materials Analysis by Ion Channeling, Academic Press, New York, 1982. p. 117.
[30] R. Cooper, K.L. Smith, M. Colella, E.R. Vance, M. Phillips, J. Nucl. Mater. 289 (2001) 199.
[31] K.L. Smith, M. Collela, R. Cooper, E.R. Vance, J. Nucl. Mater. 321 (2003) 19.
[32] K.L. Smith, N.J. Zaluzec, J. Nucl. Mater. 336 (2005) 261.
[33] Y. Zhang, W.J. Weber, H.J. Whitlow, Nucl. Instrum. and Meth. B 215 (2004) 48.
[34] Y. Zhang, W.J. Weber, A. Razpet, G. Possnert, Nucl. Instrum. and Meth. B 227 (2005) 479.
[35] Y. Zhang, W.J. Weber, Appl. Phys. Lett. 83 (2003) 1665.
[36] Y. Zhang, W.J. Weber, C.M. Wang, Phys. Rev. B 69 (2004) 205201.
[37] Y. Zhang, W.J. Weber, D.E. McCready, D.A. Grove, J. Jensen, G. Possnert, Appl. Phys. Lett. 87 (2005) 104103.
[38] Y. Zhang, W.J. Weber, D.A. Grove, J. Jensen, G. Possnert, Nucl. Instrum. and Meth. B 250 (2006) 62.
[39] Y. Zhang, J. Jensen, G. Possnert, D.A. Grove, D.E. McCready, B.W. Arey, W.J. Weber, Nucl. Instrum. and Meth. B 249 (2006) 18.
[40] R. Greco, A. Luce, Y. Wang, L. Shao, Nucl. Instrum. and Meth. B 261 (2007) 538.
[41] M. Kokkoris, G. Perdikakis, S. Kossionides, S. Petrovi, R. Vlastouc, R. Grötzschel, Nucl. Instrum. and Meth. B 219&220 (2004) 226.
[42] R. Nipoti, F. Letertre, Mat. Res. Soc. Symp. Proc. vol. 742 © 2003 Materials Research Society, K2.12
[43] P. Sigmund et al., J. ICRU Rep. 73 (2005).
[44] H. Paul, <http://www.exphys.uni-linz.ac.at/stopping/>.
[45] P.L. Grande, G. Schiwietz, Phys. Rev. A 58 (1998) 3796.
[46] H. Paul, A. Schinner, Nucl. Instrum. and Meth. B 209 (2003) 252.
[47] J.F. Ziegler, Nucl. Instrum. and Meth. B 219&220 (2004) 1027.
[48] P. Sigmund, Springer Tracts in Modern Physics, vol. 204, Springer, Heidelberg, Berlin, 2004.
[49] P. Sigmund, Mat. Fys. Medd. Dan. Vid. Selsk. 52 (2006) 557.
[50] P. Sigmund, Eur. Phys. J. D 47 (2008) 45.
[51] A. Meldrum, L.A. Boatner, W.J. Weber, R.C. Ewing, J. Nucl. Mater. 300 (2002) 242.
[52] A. Meldrum, L.A. Boatner, R.C. Ewing, Nucl. Instrum. and Meth. B 141 (1998) 347.
[53] Y. Zhang, I.-T. Bae, W.J. Weber, Nucl. Instrum. and Meth. B 266 (2008) 2828.